

## Article

# Simulation and Experimental Study of Hot Deformation Behavior in Near $\beta$ Phase Region for TC21 Alloy with a Forged Structure

Xuanming Ji <sup>1</sup>, Qimei Tian <sup>1</sup>, Yuanbiao Tan <sup>1,\*</sup> , Chaowen Huang <sup>1</sup> , Mingpan Wan <sup>1</sup> and Rudong Li <sup>2</sup>

<sup>1</sup> Guizhou Key Laboratory of Materials Mechanical Behavior and Microstructure, Guizhou University, Guiyang 550025, China; tianqimei18@163.com (Q.T.); cwhuang@gzu.edu.cn (C.H.); mpwan@gzu.edu.cn (M.W.)

<sup>2</sup> Guizhou Anda Aviation Forging Co., Ltd., Anshun 561005, China; rdli2023@163.com

\* Correspondence: ybtan1@gzu.edu.cn; Tel.: +86-147-8515-8006

**Abstract:** Quasi-beta processing was considered to be a promising processing method to obtain a component with excellent mechanical properties. To achieve an optimized quasi-beta processing parameter for TC21 alloys, the hot deformation behavior in the near  $\beta$  phase region for the alloy with a forged structure was investigated by the thermal compression test and finite element (FEM) simulation. The obtained results indicated that the flow behavior of the samples was significantly influenced by the hot deformation parameters, and it exhibited a flow hardening behavior at the start stage of deformation. Based on the experimental data, the constitutive equation and processing maps were obtained. The optimum hot processing parameter was  $986\text{ }^{\circ}\text{C}/10^{-3}\text{ s}^{-1}$ . Based on the FEM simulation results, the evolution of the temperature field, strain field, and stress field in the deformed samples at different strains exhibited a similar trend in the unstable region, which was distributed symmetrically along the center line of the samples, with the center area of the samples being the highest and the center area of the section being the lowest.

**Keywords:** TC21 alloy; hot compression; FEM simulation; flow behavior; processing map



**Citation:** Ji, X.; Tian, Q.; Tan, Y.; Huang, C.; Wan, M.; Li, R. Simulation and Experimental Study of Hot Deformation Behavior in Near  $\beta$  Phase Region for TC21 Alloy with a Forged Structure. *Crystals* **2023**, *13*, 1524. <https://doi.org/10.3390/cryst13101524>

Academic Editor: Benilde F.O. Costa

Received: 9 September 2023

Revised: 14 October 2023

Accepted: 18 October 2023

Published: 20 October 2023



**Copyright:** © 2023 by the authors. Licensee MDPI, Basel, Switzerland. This article is an open access article distributed under the terms and conditions of the Creative Commons Attribution (CC BY) license (<https://creativecommons.org/licenses/by/4.0/>).

## 1. Introduction

TC21 alloys with excellent strength, fracture toughness, high damage tolerance, and low crack growth rate have been widely applied to manufacture the key components in the engines and airframes of aircraft [1–4]. The components of TC21 alloys were usually processed by hot working technology [5–7]. The mechanical property of the parts is dependent on the deformed microstructure during hot processing, which is mainly associated with hot deformation parameters. To achieve parts with high performance, it is extremely critical to fundamentally comprehend the hot deformation characteristics of TC21 alloys so as to govern the final deformed microstructure of the alloy subjected to hot working.

Recently, numerous studies have been reported to reveal the hot deformation characteristics of Ti alloys [8–13]. Zhang et al. [8] studied the hot deformation behavior and the microstructure evolution mechanism of TC19 titanium alloy, discovering that the deformation mechanisms were dynamic recovery and dynamic recrystallization, and the instability region always had a high strain rate. When the strain rate was high, the sub-grain rotated continuously to transform from low-angle grain boundaries into high-angle grain boundaries. Qiu et al. [9] performed the isothermal hot compression tests on SP700 titanium alloy, drawing the conclusion that the best processing parameter range of SP700 titanium alloy was  $775\text{--}825\text{ }^{\circ}\text{C}$  for deformation temperature and  $0.3\text{--}1\text{ s}^{-1}$  and  $0.001\text{--}0.002\text{ s}^{-1}$  for strain rate. Super-plastic deformation may happen under the deformation conditions of  $800\text{ }^{\circ}\text{C}/0.001\text{ s}^{-1}$  and  $800\text{ }^{\circ}\text{C}/1\text{ s}^{-1}$  with a strain of 0.9. Gao et al. [10] investigated the flow behavior and microstructure evolution of TA15 titanium alloy with a nonuniform

microstructure. The results show that lamellar  $\alpha$  undertakes most of the deformation and turns to be rotated, bent, and globularized. Wang et al. [12] also investigated the flow stress curves and established the Arrhenius constitutive model and processing maps of Ti-4.2Al-0.005B titanium alloy. Li et al. [13] studied the flow behavior and globularization kinetics of a TC6 alloy by a set of internal state variable-based unified viscoplastic constitutive equations.

Nevertheless, only a few studies in the literature on the hot deformation behavior of TC21 alloys were reported [14–17]. Zhao et al. [14] reported the hot working characteristics of TC21 alloys with a cluster of  $\alpha$  block structure in the  $\alpha + \beta$  field. The results show that the  $\alpha$  block structure disappeared during hot deformation and two stable domains with peak efficiencies of power dissipation were found to be at 880–900 °C/1–10 s<sup>−1</sup> and 925–950 °C/0.32–10 s<sup>−1</sup>, respectively. This suggests that a high strain rate is beneficial to the hot working of TC21 alloys with a cluster of  $\alpha$  block structure in the  $\alpha + \beta$  region. Zhu et al. [5,15] investigated the hot deformation characteristics of as-cast TC21 alloys with lamellar  $\alpha$  colonies in the  $\beta$  area and found that two regions of peak efficiency were observed to be 1000 °C/0.01 s<sup>−1</sup> and 1150 °C/0.01 s<sup>−1</sup>, respectively. The deformation mechanism is related to the dynamic recrystallization of the  $\beta$  phase. For the TC21 alloy with a bimodal microstructure, the optimal processing domain is at the temperature of 880–900 °C/0.001–0.03 s<sup>−1</sup>, which reveals that a low strain rate is advantageous to the hot processing of the alloy [16]. For the TC21 alloy with a widmanstätten structure, Wang et al. [17] found that lamellar  $\alpha$  was crushed into the short bar-like  $\alpha$  phase during hot working in the  $\alpha + \beta$  field. These results show that the differences in the initial microstructure and processing region can result in a significant difference in the optimal processing region and microstructure evolution.

Recently, Shi et al. [18] found that three-state microstructures composed of equiaxed  $\alpha$  phase, lamellar  $\alpha$  phase, and transformed  $\beta$  matrix can be obtained for a TC21 alloy forged by quasi- $\beta$  forging method ( $T_{\beta} + 10$ –30 °C), which can give rise to more excellent mechanical properties compared with that of a TC21 alloy forged by  $\alpha + \beta/\beta$  forging method. However, there is no information on the hot deformation characteristics and microstructure evolution of a TC21 alloy forged during quasi- $\beta$  forging ( $T_{\beta} + 10$ –30 °C). To obtain an optimized quasi-beta processing parameter and govern the final microstructure of a TC21 alloy after quasi- $\beta$  forging, a TC21 alloy with equiaxed  $\alpha$  structure was hot-compressed in the range of 966–986 °C and 0.001–10 s<sup>−1</sup> in this work, and the optimization processing parameters of the alloy during quasi- $\beta$  forging was achieved by FEM method and experimental investigation.

## 2. Materials and Experimental Procedures

The samples used in this study were a forged TC21 alloy with a diameter of 80 mm, and the temperature of  $\beta \rightarrow \alpha + \beta$  was determined to be 961 °C based on the optical metallography [19]. The chemical composition of TC21 alloy is depicted in Table 1. The microstructure of the as-received samples consisted of equiaxed  $\alpha$ , lamellar  $\alpha$ , and retained  $\beta$  phase, as exhibited in Figure 1.

**Table 1.** The chemical composition of the samples.

Element	Al	Mo	Nb	Sn	Zr	Cr	Si	Fe	C	O	N	Ti
Content (wt%)	6.28	3.06	1.89	2.04	2.18	1.61	0.066	0.022	0.009	0.122	0.005	Balance

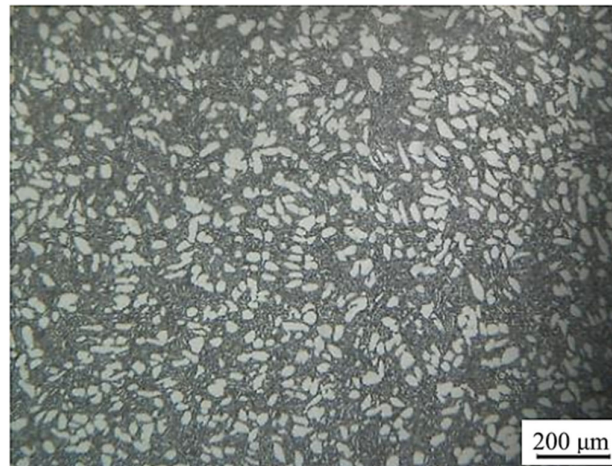


**Figure 1.** Microstructure of the TC21 alloy with a forged microstructure.

The samples for the hot compression were processed from the forged bars, and the size of the sample was  $\varnothing 8 \text{ mm} \times 12 \text{ mm}$ . A Gleeble-3500 thermo-mechanical simulator was used to operate the isothermal compression tests. For the purpose of addressing the flow behavior and microstructure evolution of TC21 alloy after quasi- $\beta$  forging, three deformation temperatures of 966 °C, 976 °C, and 986 °C were adapted, and the strain rate was set as  $0.001 \text{ s}^{-1}$ – $10 \text{ s}^{-1}$ . The true strain was set as 1.2. The samples were heated to a designated temperature and held for 5 min to keep the temperature homogeneous before hot compression. All deformed samples were rapidly water-cooled after hot deformation to keep the microstructure under high temperatures. The sketch diagram of hot deformation tests is demonstrated in Figure 2. A thermocouple spot was used to control the temperature, which was welded at the mid-span of the samples. In order to reduce the friction between the cylindrical sample and the tool, the graphite lubricant was used to coat the top and bottom surfaces of samples, and tantalum foils of 0.1 mm were set between the cylindrical samples and the tool.

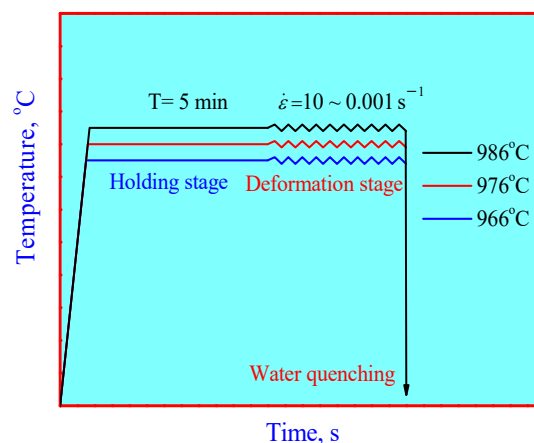


**Figure 2.** Sketch diagram of hot deformation tests.

All the experiment samples were sectioned parallel to the compression axis to observe the microstructure on optical microscope (OM) (Leica Instruments GmbH, Wetzlar, Germany). For optical examination, the samples were ground, mechanically polished, and chemically etched with a Kroll reagent, whose ingredient is 5 (vol.%) HF + 25 (vol.%) HNO<sub>3</sub> + 70 (vol.%) H<sub>2</sub>O. Based on the results obtained from the experiment, the temperature, strain, and stress field of TC21 alloy with a forged microstructure deformed at different processing parameters were simulated by FEM method.

### 3. Results and Discussion

#### 3.1. Flow Curves

##### 3.1.1. Adiabatic Correction

When the strain rate is high ( $\geq 1 \text{ s}^{-1}$ ), the deformation time is short, and the heat cannot be diffused in time, resulting in uneven temperature of the sample, and the thermocouple can only measure the surface temperature of the sample. This made the measured data inaccurate, so we corrected the temperature. The temperature rise can be expressed by the following equation [20]:

$$\Delta T = \frac{0.95\eta \int_0^\epsilon \sigma d\epsilon}{\rho c} \quad (1)$$

where  $\Delta T$  is the change in temperature in the hot compression processing,  $\int_0^\epsilon \sigma d\epsilon$  is the plastic deformation work,  $\rho$  is the density ( $4.5 \text{ g}\cdot\text{cm}^{-3}$ ),  $c$  is the specific heat capacity ( $612 \text{ J}\cdot(\text{Kg}\cdot^\circ\text{C})^{-1}$ ), and  $\eta$  is the adiabatic correction coefficient. If the strain rate is less than  $0.001 \text{ s}^{-1}$ , the value of  $\eta$  will be 0, and if the strain rate is more than  $1 \text{ s}^{-1}$ ,  $\eta$  will be 0.95. When the strain rate is between  $0.001 \text{ s}^{-1}$  and  $1 \text{ s}^{-1}$ , we can calculate  $\eta$  with the following equation [21]:

$$\eta = 0.316 \log(\dot{\epsilon}) + 0.95 \quad (2)$$

The effect of temperature rise on flow stress can be calculated by the following formula proposed by Devadas [22]:

$$\Delta\sigma = \frac{Q}{n\alpha R} \left( \frac{1}{T} - \frac{1}{T + \Delta T} \right) \quad (3)$$

where  $\Delta\sigma$  is the effect of temperature rise on flow stress,  $Q$  is the hot deformation activation energy,  $R$  is the universal gas constant,  $n$  is the stress exponent,  $\alpha$  is the material constant, and  $T$  is the deformation temperature in Kelvin. The values of  $Q$ ,  $n$ , and  $\alpha$  can be calculated by the Arrhenius type equation, whose mathematical expression is as follows [23]:

$$\dot{\epsilon} = A [\sinh(\alpha\sigma_p)]^n \exp\left(-\frac{Q}{RT}\right) \quad (4)$$

where  $\sigma_p$  indicates the peak stress,  $\dot{\epsilon}$  represents the strain rate, and  $A$  is the material constants. By taking the logarithm and fitting Equation (4), we can obtain that the values of  $n$ ,  $\alpha$ , and  $Q$  are 2.649, 0.0225 and 621.16 kJ, respectively. Then, we can evaluate the  $\Delta\sigma$  during different hot deformation conditions.

##### 3.1.2. Friction Correction

The friction cannot be eliminated completely, although the lubricants and tantalum foils were used to reduce the friction, especially at the condition of high deformation temperature. Therefore, we corrected the experimental data with the following equation [24]:

$$\sigma = \frac{PC^2}{2(\exp(C) - 2C - 1)} \quad (5)$$

where  $P$  represents the experimental flow stress, and  $C$  is the correction coefficient of sample–anvil interface friction, which can be calculated as follows:

$$C = \frac{2mR}{H} \quad (6)$$

where  $H$  is the height of the sample after deformation,  $R$  is the bulge radius of the cylinder after compression, and  $m$  indicates the friction coefficient. The  $m$  is expressed by the following:

$$m = \frac{\left(\frac{R}{H}\right)b}{4/\sqrt{3} - (2b/3\sqrt{3})} \quad (7)$$

Parameter  $b$  can be determined as follows:

$$b = 4 \frac{H}{\Delta H} \frac{\Delta R}{R} \quad (8)$$

In the above equation,  $\Delta H$  can be calculated by  $H - H_0$ , where  $H_0$  is the initial height of the sample and  $\Delta R$  is the difference between the bulge radius and bottom radius of the cylinder after compression. Using Equations (5)–(8), we can obtain the stress after friction correction.

### 3.1.3. True Stress–Strain Curves

The true stress–strain curves gained from the hot compression tests of the forged TC21 alloy are exhibited in Figure 3. It can be found that the curves exhibited a flow hardening behavior, and the flow stress increased with the rise of strain. At a given processing temperature, higher strain rates can lead to a higher flow stress. It is noted that when the strain rate was  $1 \text{ s}^{-1}$ , the flow stress exhibited a small decrease at the beginning of the flow curve. This phenomenon can be explained by the dynamic theory [25], which suggests that the mobile dislocations rapidly formed from grain boundary sources at the beginning of hot deformation can quickly move from the grain boundary to the interior of the grain, and then result in a decrease in the flow stress [25,26].

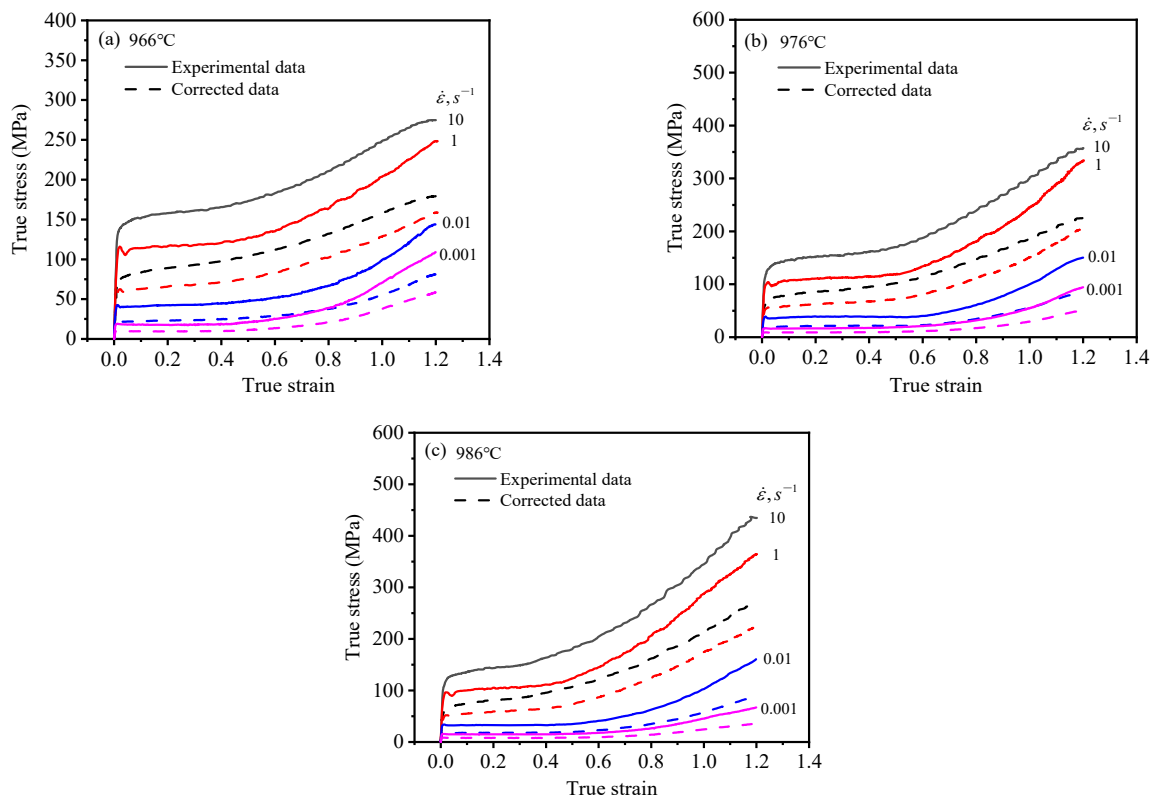


**Figure 3.** True stress–strain curves for the samples at deformation temperatures of (a) 966 °C, (b) 976 °C, and (c) 986 °C before and after correction, respectively. (A color in the stress–strain curves is corresponded to a given strain rate).

The flow curves before and after correction are also shown in Figure 3. It can be concluded that the temperature rise and the friction can affect the stress significantly, especially in the condition of high deformation temperature and high strain rate. The difference in stress before and after correction is smallest at the deformation condition of 986 °C/ $0.001 \text{ s}^{-1}$ . The difference in stress before and after correction increases gradually with increasing strain.

### 3.2. Constitutive Parameters

There are many studies in the literature indicating that the working parameters can significantly affect the hot working behavior of the alloys [27–29]. Figures 4 and 5 show the dependence of the peak stress on hot working parameters for the forged TC21 alloy, respectively. It is obvious that increasing peak stress was observed with the augment of the strain rate and the reduction in the temperature. We used the Arrhenius type equation (Equation (4)), which can primarily predict the constitutive behavior of most alloys in hot deformation processing, to construct the relationship between hot processing parameters and flow stress [30].

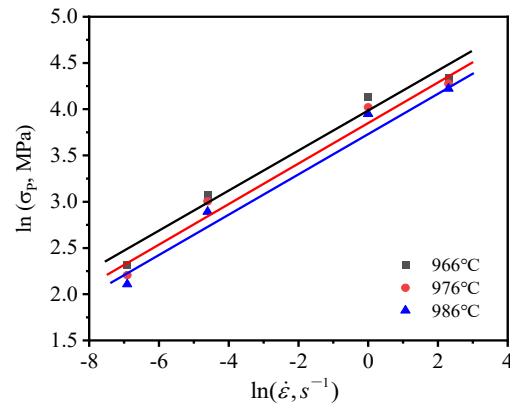


**Figure 4.** Relationship between the peak stress and strain rate (the line is a fitted line from the experimental data).

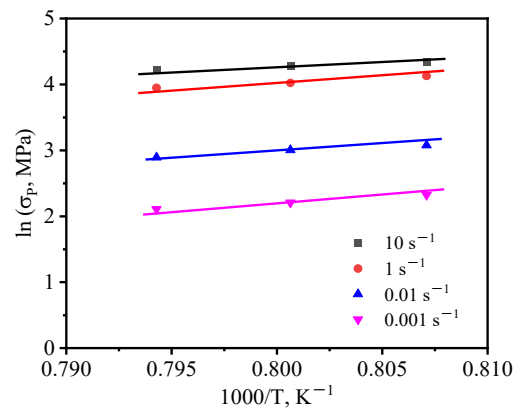


**Figure 5.** Relationship between the peak stress and deformation temperature (the line is a fitted line from the experimental data).

According to Equation (4) and the logarithm of both sides of Equation (4), we can express the following:

$$\ln \sinh(\alpha \sigma_p) = -\frac{1}{n} \ln A + \frac{1}{n} \ln \dot{\epsilon} + \frac{1}{n} \cdot \frac{Q}{RT} \quad (9)$$

The values of  $\alpha$ ,  $A$ ,  $n$ , and  $Q$  were calculated according to Ref. [31]. The value of  $\alpha$  was evaluated from the minimum residual sum of squares to be  $0.035 \text{ MPa}^{-1}$ . The values of  $A$ ,  $n$ , and  $Q$  were stemmed from the peak stress to be  $2.51 \times 10^{21} \text{ s}^{-1}$ , 3.09, and 549.121 kJ/mol, respectively.

Therefore, Equation (4) can be expressed as follows:

$$\dot{\epsilon} = 2.51 \times 10^{21} [\sinh(0.035 \sigma_p)]^{3.09} \exp\left(-\frac{549121}{RT}\right) \quad (10)$$

To determine the model, a figure of  $\ln(Z)$  was obtained versus  $\ln(\sinh(\alpha\sigma_p))$  (Figure 6). It can be observed that the peak stress rose with the increase in the  $Z$  parameter (Zener–Hollomon), and they appeared to have a good linear relationship. Therefore, the established constitutive equation was valid for the forged samples.

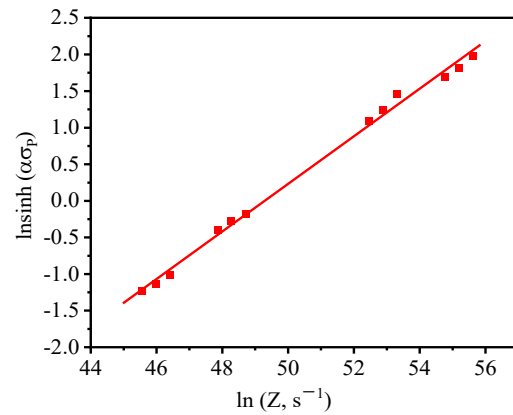


**Figure 6.** Relationship between the peak stress ( $\sigma_p$ ) and the  $Z$  parameter.

The constitutive equation calculated above is based on the peak stress, and the true strain also has an effect on the flow behavior, so we calculated the constitutive equation under different strains. In addition, the calculated flow stress under each strain was obtained by the following equation [32]:

$$\sigma = \frac{1}{\alpha} \ln \left\{ \left( \frac{Z}{A} \right)^{\frac{1}{n}} + \left[ \left( \frac{Z}{A} \right)^{\frac{2}{n}} + 1 \right]^{\frac{1}{2}} \right\} \quad (11)$$

Figure 7 is the comparison between the calculated flow stress and the experimental flow stress. It can be seen that the difference between the calculated data and the experimental data is small and that it increases as the true strain increases. Furthermore, the correlation coefficient ( $R^2$ ) is usually used to reflect the capability of the linear relationship between the calculated and the experimental data. It can be seen from Figure 8 that the  $R^2$  is 0.976 between the calculated and the experimental data, indicating that the proposed constitutive equation in this paper exhibits an excellent fit with the measured values.

### 3.3. Processing Maps

A processing map is an efficient method to reveal the mechanism of hot deformation and optimize the parameters of hot processing and is composed of the superposition of the energy dissipation diagram and instability diagram [33,34]. The power dissipation efficiency ( $\eta$ ) changes when changing the hot processing parameters, and it can be described as follows [35,36]:

$$\eta = \frac{J}{J_{\max}} = \frac{2m}{m+1} \quad (12)$$

where  $m$  is the strain rate sensitivity index. The instability diagram consists of the instability criterion ( $\zeta$ ), which can be defined by Equation (12) [32]:

$$\zeta = \frac{\partial \lg \left[ \frac{m}{m+1} \right]}{\partial \lg \dot{\epsilon}} + m < 0 \quad (13)$$

when the  $\zeta$  is negative, the flow instabilities most commonly take place as localizations in the flow curve. Based on the principles of the dynamics materials model (DMM) [37,38], the processing maps were proposed at different strains to obtain the optimum hot compression parameters for the samples with a forged structure, as shown in Figure 9. The shaded

regions were on behalf of the instability regions, and the contour number indicated the efficiency of power dissipation.

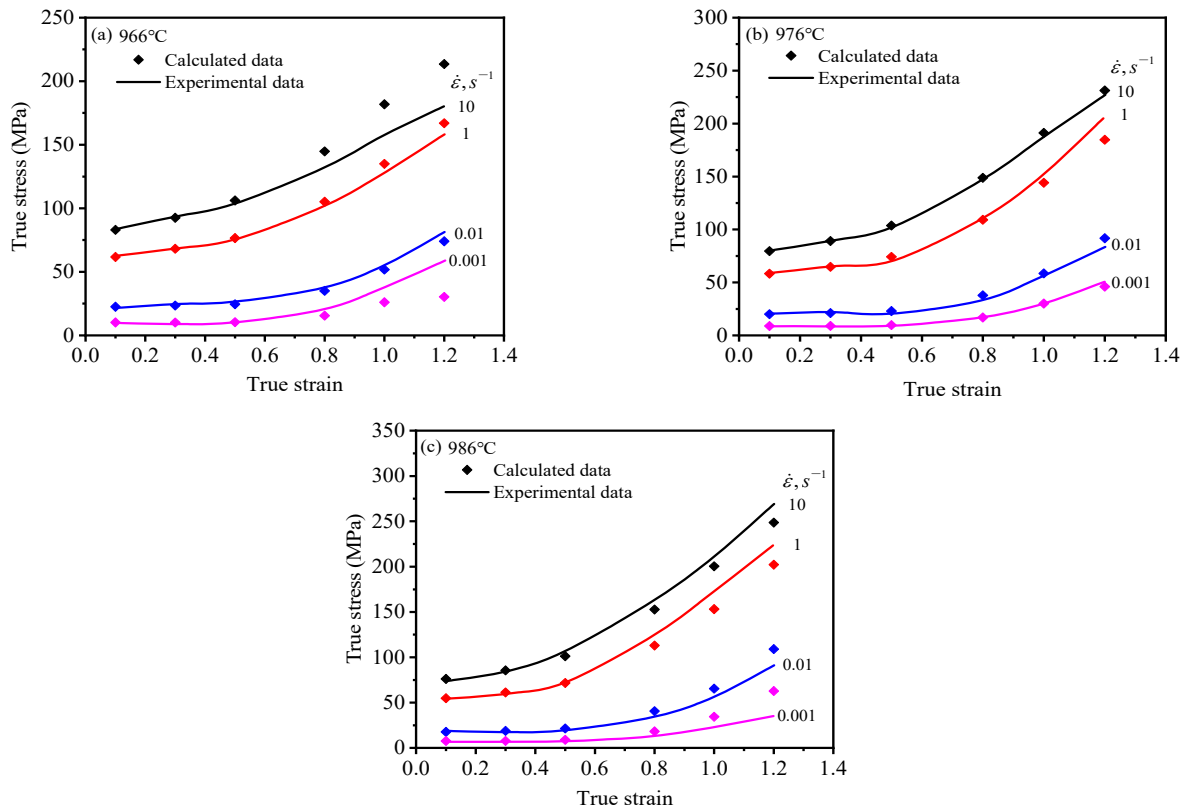


**Figure 7.** The comparison between the calculated data and experimental data at deformation temperatures of (a) 966 °C, (b) 976 °C, and (c) 986 °C.

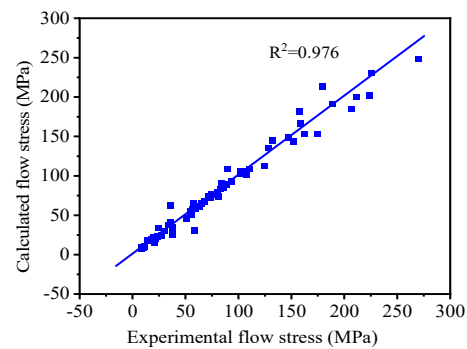


**Figure 8.** Correlation between the calculated and experimental flow stress for the strain range of 0.1–1.2 over the entire strain rate ( $10 s^{-1}$ – $0.001 s^{-1}$ ) and deformation temperature range (966–986 °C).

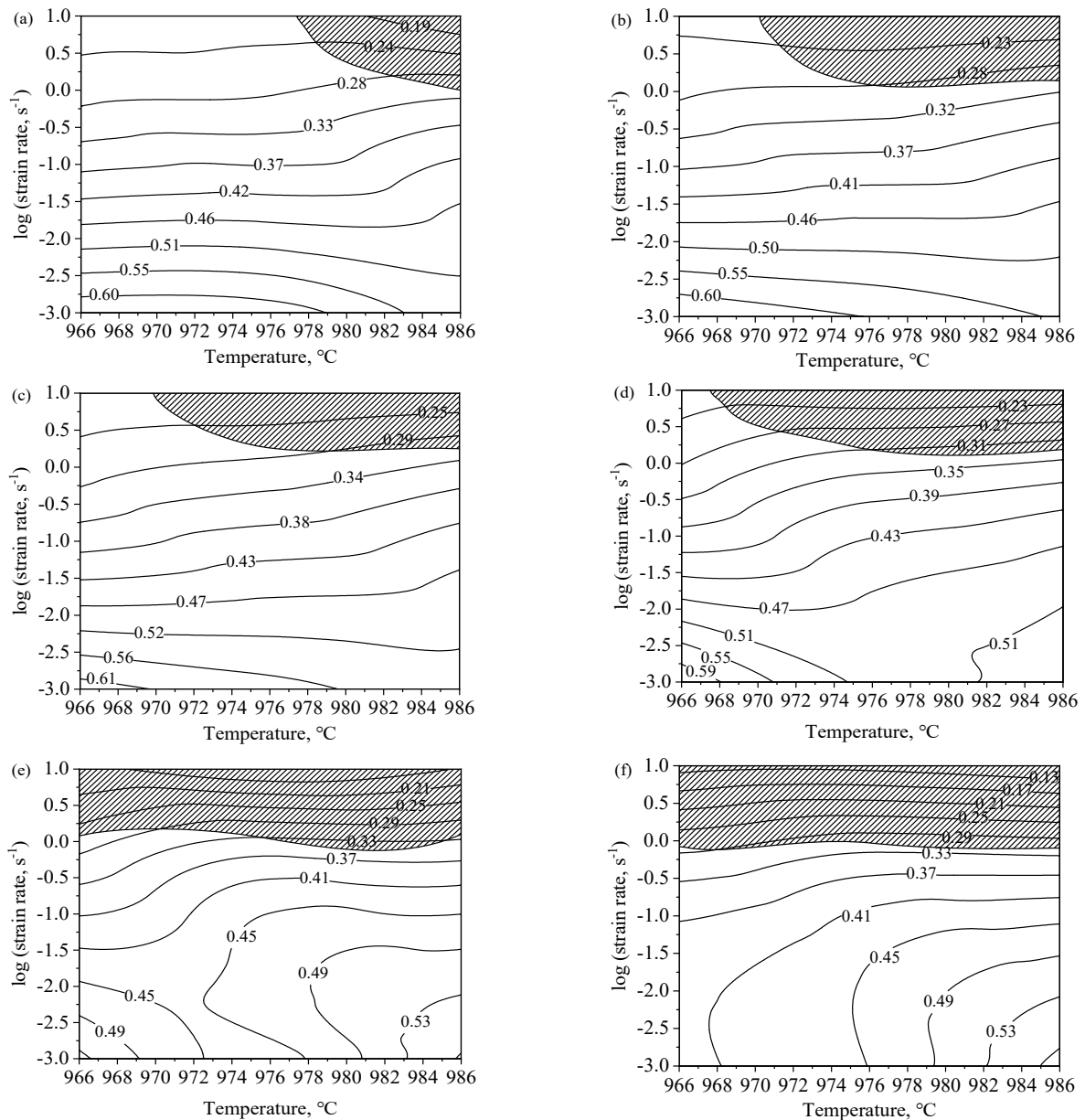


**Figure 9.** Processing maps for the deformed samples at the true strains of (a) 0.2, (b) 0.3, (c) 0.4, (d) 0.5, (e) 0.6, and (f) 0.8.

When the strain rate was higher than about  $1 \text{ s}^{-1}$ , and the temperature range was  $976\text{--}986 \text{ }^\circ\text{C}$ , the flow instability phenomenon can be observed at the strain of 0.2. The domain with a peak value of  $\eta$  took place in the region of  $966\text{--}979 \text{ }^\circ\text{C}$  and  $1.7 \times 10^{-3}\text{--}10^{-3} \text{ s}^{-1}$ , and the peak value of  $\eta$  was about 0.60. Generally, a high value of  $\eta$  is associated with superplasticity and dynamic recrystallization (DRX). For Ti alloys, the DRX of  $\beta$  phase can occur when the value of  $\eta$  is higher than 0.45 [39]. Thus, the deformation mechanism of TC21 alloys with a forged structure is associated with the DRX of the  $\beta$  phase in the near  $\beta$  phase region. With the increase in strain from 0.2 to 0.8, the area of flow instability expanded, and the region with peak efficiency of power dissipation changed, which gradually moved to the domain with a high temperature and low strain rate. On the basis of the above analysis, it can be concluded that the optimum hot processing parameter was  $986 \text{ }^\circ\text{C}/10^{-3} \text{ s}^{-1}$ .

### 3.4. Microstructure after Hot Deformation

In order to determine the deformation mechanism of the forged TC21 alloy at different hot deformation conditions, the microstructures after hot compression were characterized, as exhibited in Figure 10. At the strain rate of  $1 \text{ s}^{-1}$ , the grains were obviously elongated along the radial direction, and the grain size increased with the rising temperature. It was also found that there were some fine recrystallized grains of  $\beta$  phase along the strip grains, indicating that dynamic recrystallization occurred for the  $\beta$  phase grains. At the deformation temperature of  $966 \text{ }^\circ\text{C}$ , a full dynamic recrystallization took place in the deformed alloys at the strain rate of  $0.01 \text{ s}^{-1}$ , and the grains were significantly refined. When increasing the temperature from  $966$  to  $986 \text{ }^\circ\text{C}$  with a strain rate of  $0.001 \text{ s}^{-1}$ , the recrystallized grains were obviously coarsened due to a high recrystallization drive at high deformed temperature and sufficient deformation time.

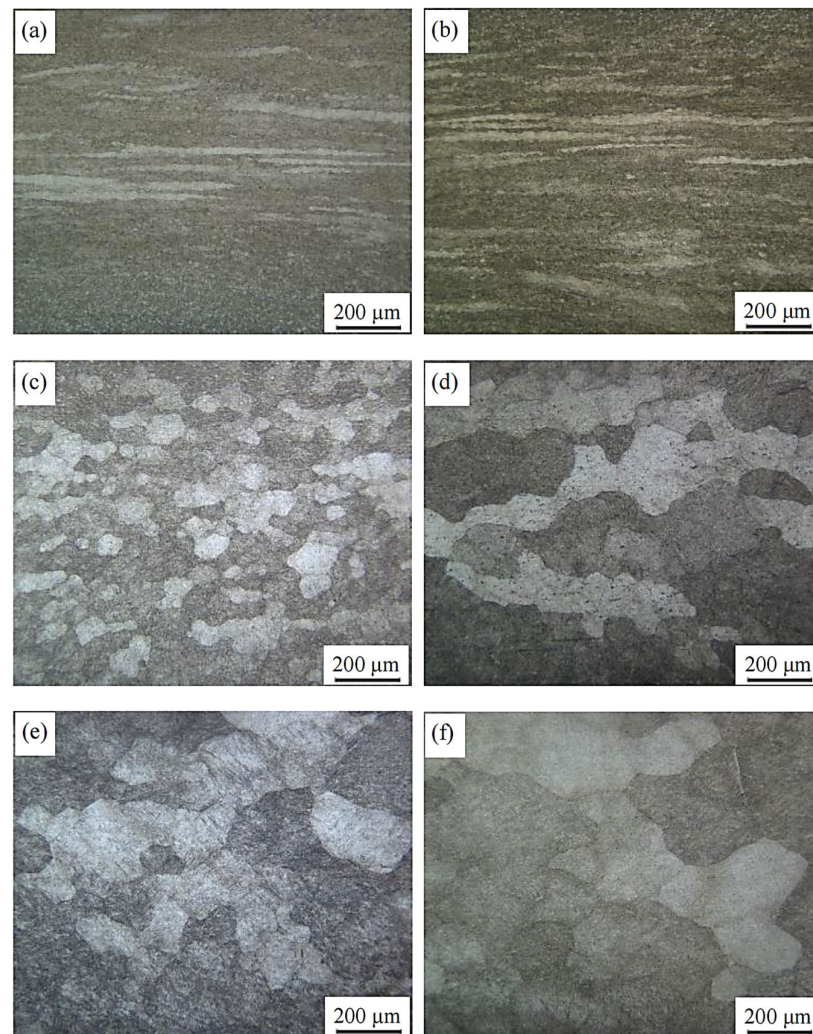


**Figure 10.** Optical microstructures of the alloys with a true strain of 1.2 at different conditions: (a)  $976 \text{ }^\circ\text{C}/1 \text{ s}^{-1}$ , (b)  $986 \text{ }^\circ\text{C}/1 \text{ s}^{-1}$ , (c)  $966 \text{ }^\circ\text{C}/0.01 \text{ s}^{-1}$ , (d)  $966 \text{ }^\circ\text{C}/0.001 \text{ s}^{-1}$ , (e)  $976 \text{ }^\circ\text{C}/0.001 \text{ s}^{-1}$ , and (f)  $986 \text{ }^\circ\text{C}/0.001 \text{ s}^{-1}$ .

### 3.5. Finite Element Simulation of the Samples Deformed at Different Parameters

In order to fully understand the evolution of the temperature field and strain field of the TC21 alloy in hot compression processing, this study used the Deform-3D finite element simulation software to simulate the hot compression process of the forged TC21 alloy. The cylindrical model was built by the SolidWorks software, and the size of the model is the same as the size of the experimental samples. Then, the model was imported into the

Deform-3D software and divided into 32,000 grids. The workpiece was set as a plastic body and the dies were set as a rigid body because the elastic deformation was usually ignored during the plastic deformation of the workpiece at high temperatures [40,41]. During the simulation, the top die moved along the central axis of the cylindrical samples and the lower die did not move. To ensure the precision of the FE simulation, the temperature of the workpiece was set at the same temperature as the experimental temperature. Moreover, the shear friction factor between the cylindrical workpiece and the tools was set as 0.3, and the heat transfer coefficient was set to 5 N/S/mm/°C. To analyze the evolution in temperature and strain of the entire sample, the three positions shown in Figure 11 were selected for analysis.

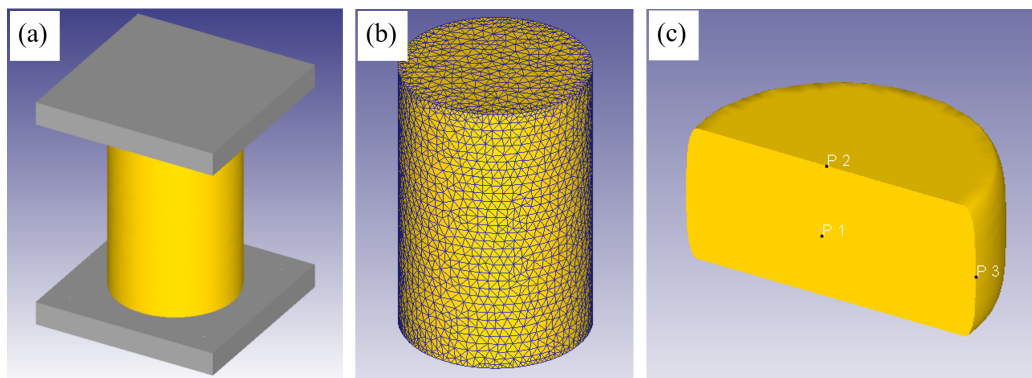


**Figure 11.** Schematic diagram of finite element simulation for upsetting (a) geometric model, (b) grid division, and (c) node location.

### 3.5.1. Temperature Field Simulation

The optimal hot working parameters and unstable hot deformation parameters of the TC21 alloy were obtained from the hot processing maps, which were  $986\text{ °C}/0.001\text{ s}^{-1}$  and  $986\text{ °C}/10\text{ s}^{-1}$ , respectively. In order to study the evolution of the temperature field of the samples during hot compression in stable and unstable regions, the simulation of the temperature field in stable and unstable regions is illustrated in Figures 12 and 13.

It can be found that the temperature of the sample dropped at first and then rose slightly at the deformation condition of  $986\text{ °C}/0.001\text{ s}^{-1}$ . This is associated with the fact that the heat exchange occurs between the mold and the deformed sample, which results in a decrease in the temperature of the deformed samples at the initial stage of deformation. The temperature evolution situation of the three positions was similar, and the temperature difference was not large, which was not more than  $30\text{ °C}$ . When increasing the true strain, the temperature of the sample increased slightly, and the temperature difference decreased gradually. This can mainly be attributed to the strain rate being low, resulting in sufficient heat transfer, good thermal diffusivity, stable microstructure after compression, and uniform overall performance of the sample. It can be seen from Figure 10 that a homogeneous microstructure with full dynamic crystallized grains can be obtained when the samples are deformed at  $986\text{ °C}/0.001\text{ s}^{-1}$  and a true strain of 1.2.

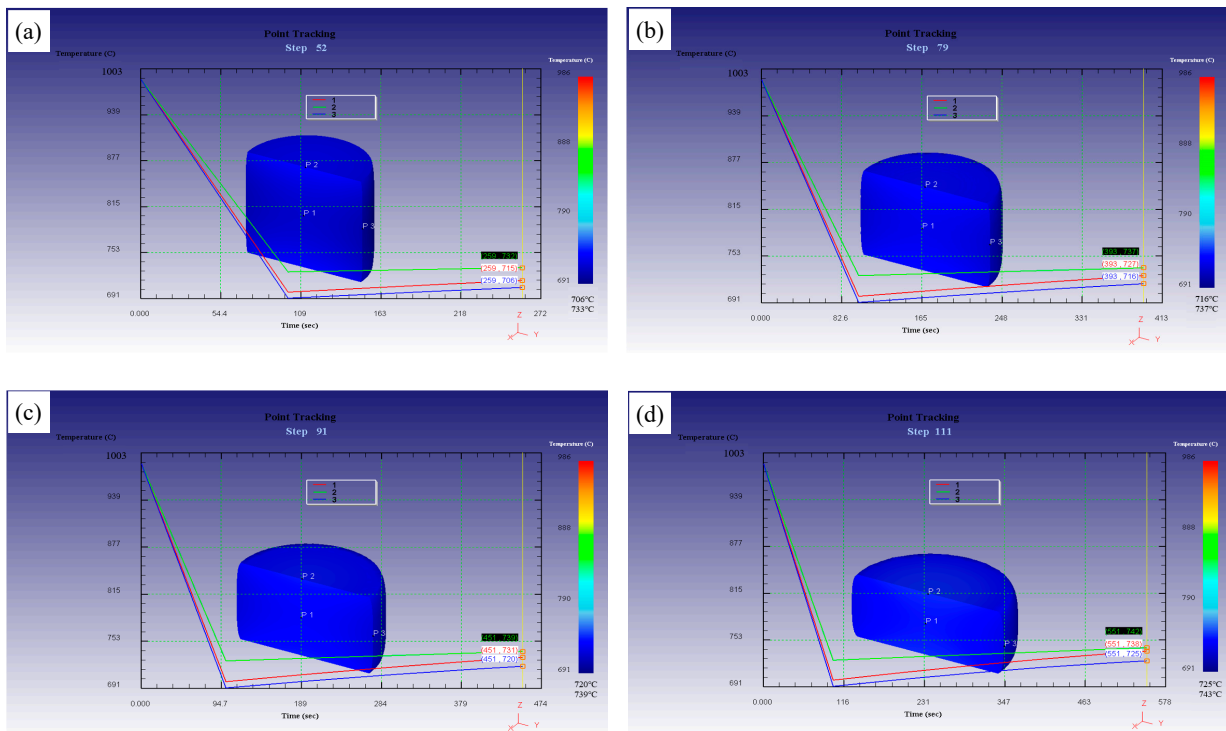


**Figure 12.** Temperature field of the deformed samples at  $986\text{ }^{\circ}\text{C}/0.001\text{ s}^{-1}$ : (a) 0.3, (b) 0.5, (c) 0.6, and (d) 0.8.

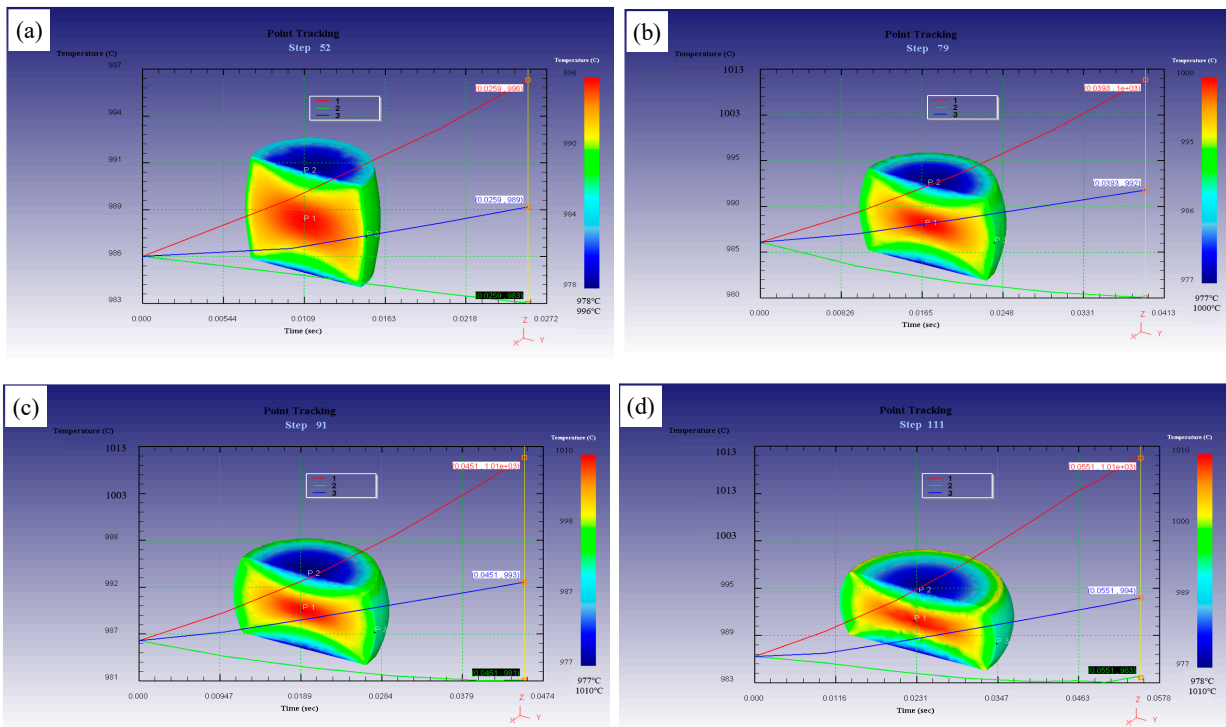


**Figure 13.** Temperature field of the deformed samples at  $986\text{ }^{\circ}\text{C}/10\text{ s}^{-1}$ : (a) 0.3, (b) 0.5, (c) 0.6, and (d) 0.8.

When the deformation condition was  $986\text{ }^{\circ}\text{C}/10\text{ s}^{-1}$ , the temperature at P1 (easy deformation region) and P3 (intermediate deformation region) rose rapidly with the progress of compression, and the temperature at P2 (difficult deformation region) was almost constant.

Moreover, at the end of compression, the temperature at P1 was the highest, and the temperature at P2 was the lowest. When increasing the strain, the temperature of P2 was almost constant, but the temperature at P1 was obviously increased, and the temperature difference became larger. This is mainly because the strain rate was too large, and the equivalent strain rate in different regions of the samples was different; the instability phenomenon occurred, which made the internal homogeneity of the samples poor during compression. Generally, the Ti alloys present a low heat conductivity. A significant deformation heat is easily formed when the Ti alloys are deformed at a high strain rate, which can result in a heterogeneous deformation in the deformed samples. It is seen from Figure 13 that the temperature of region P1 is obviously higher than that of regions P2 and P3. This is because region P1 easily deforms during the hot compression of the TC21 alloy, which leads to a large deformation heat and then causes an increase in the temperature. For the Ti alloys, it is commonly known that a significant deformation formed from hot compression will result in flow instability.

### 3.5.2. Effective Strain Field Simulation

Figure 14 exhibits the simulation results of the effective strain field under thermal deformation condition of  $986\text{ }^{\circ}\text{C}/0.001\text{ s}^{-1}$ ; it can be seen that the effective strain of the samples did not change during the whole compression process under any strain condition. It can be considered that the strain rate was too low, so the sample obtained a stable structure and good homogeneity after compression. Figure 15 depicts an effective strain field simulation of thermal compression at  $986\text{ }^{\circ}\text{C}/10\text{ s}^{-1}$ . It was clear that with the progress of compression, the effective strain at three positions was significantly increased, and  $P1 > P3 > P2$ , which corresponded to the deformation degree of each region. In addition, with the increase in strain, the effective strain at a given position increased, and the deformation in the effective strain at different positions also obviously increased. This suggests that a high strain rate results in a significant heterogeneous deformation.

### 3.5.3. Effective Strain Rate Field Simulation

When the thermal deformation condition is  $986\text{ }^{\circ}\text{C}/0.001\text{ s}^{-1}$ , the effective strain rate field of hot compression was simulated, as shown in Figure 16; it can be seen that with the progress of compression, the effective strain rate first rose rapidly and then rose slowly, which may be due to softening behavior. The effective strain rate was  $P1 > P3 > P2$  after compression. With the increase in strain, the effective strain rate also increased, and the difference in the effective strain rate at the three positions was always within  $0.001\text{ s}^{-1}$ , which indicates that the flow inside the sample was uniform and that the effective strain rate of each part was also uniform.

Figure 17 is a simulation of the effective strain rate field when the hot compression condition was  $986\text{ }^{\circ}\text{C}/10\text{ s}^{-1}$ ; it can draw a conclusion that the effective strain rate of P1 rose rapidly at first and then slowly, P2 tended to be gentle after the rapid increase, and P3 decreased slightly after the rapid increase to the peak. The strain rate remained as  $P1 > P3 > P2$  after the end of compression. When increasing the strain, the effective strain rate increased gradually. When the strain reached 0.8, the effective strain rate of P2 increased suddenly after becoming stable, but it was still lower than P3 and P1; this may be because the strain was too large, affecting the stability of the samples.

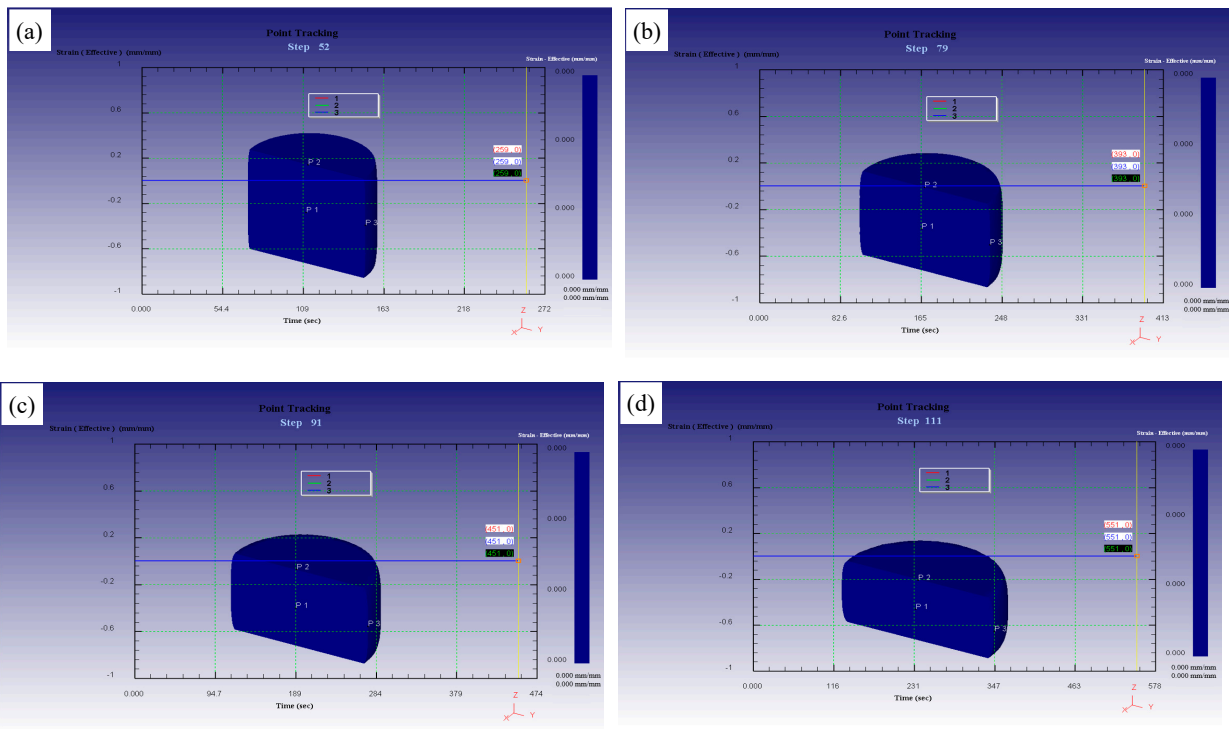


Figure 14. Effective strain field of the deformed samples at 986 °C/0.001 s<sup>-1</sup>: (a) 0.3, (b) 0.5, (c) 0.6, and (d) 0.8.

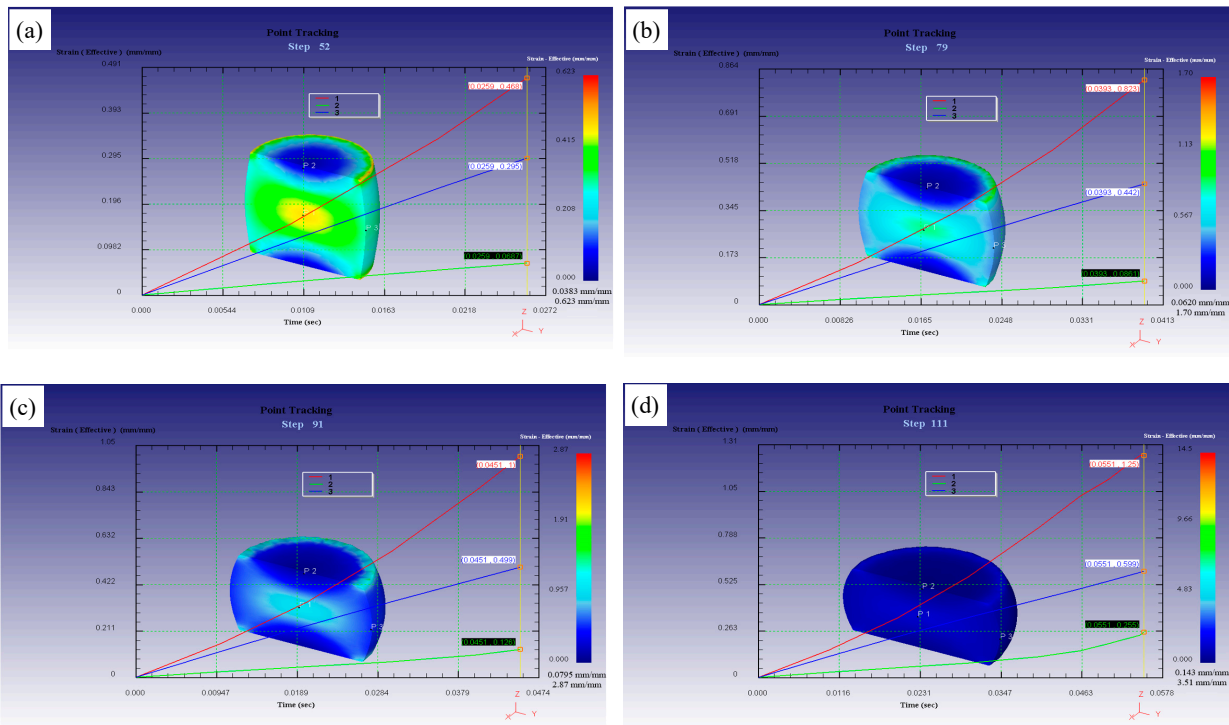


Figure 15. Effective strain field of the deformed samples at 986 °C/10 s<sup>-1</sup>: (a) 0.3, (b) 0.5, (c) 0.6, and (d) 0.8.

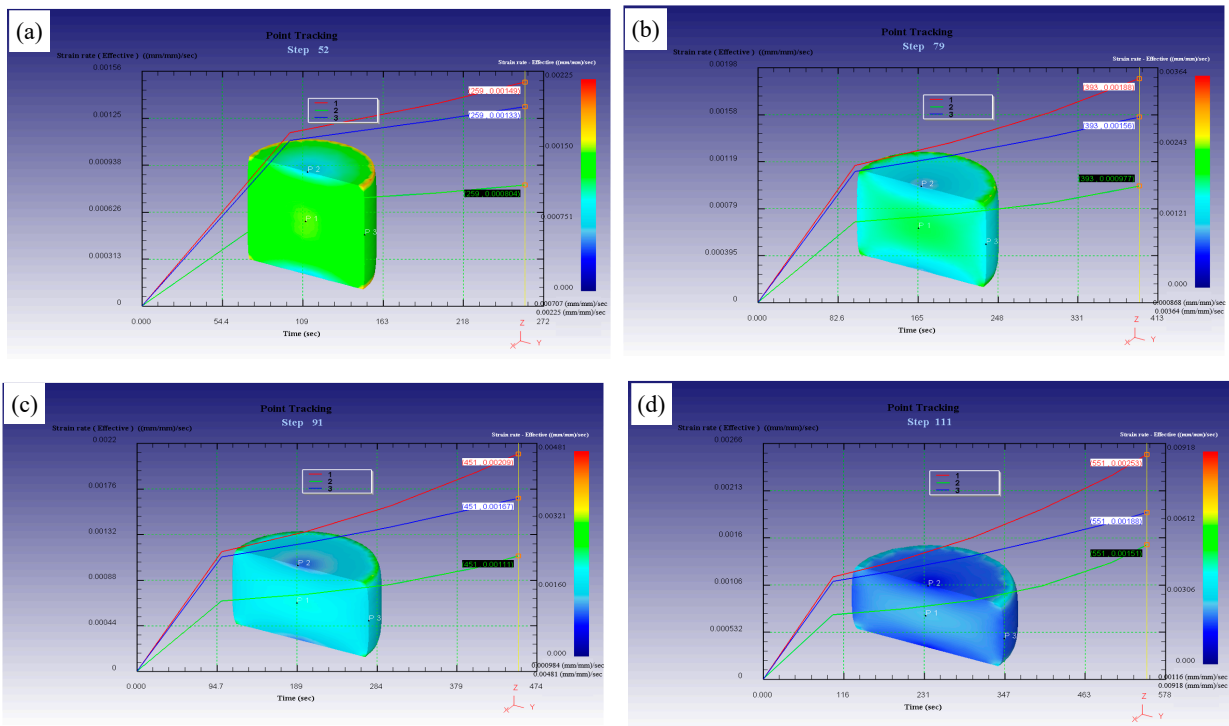


Figure 16. Effective strain rate field of the deformed samples at  $986\text{ }^{\circ}\text{C}/0.001\text{ s}^{-1}$ : (a) 0.3, (b) 0.5, (c) 0.6, and (d) 0.8.

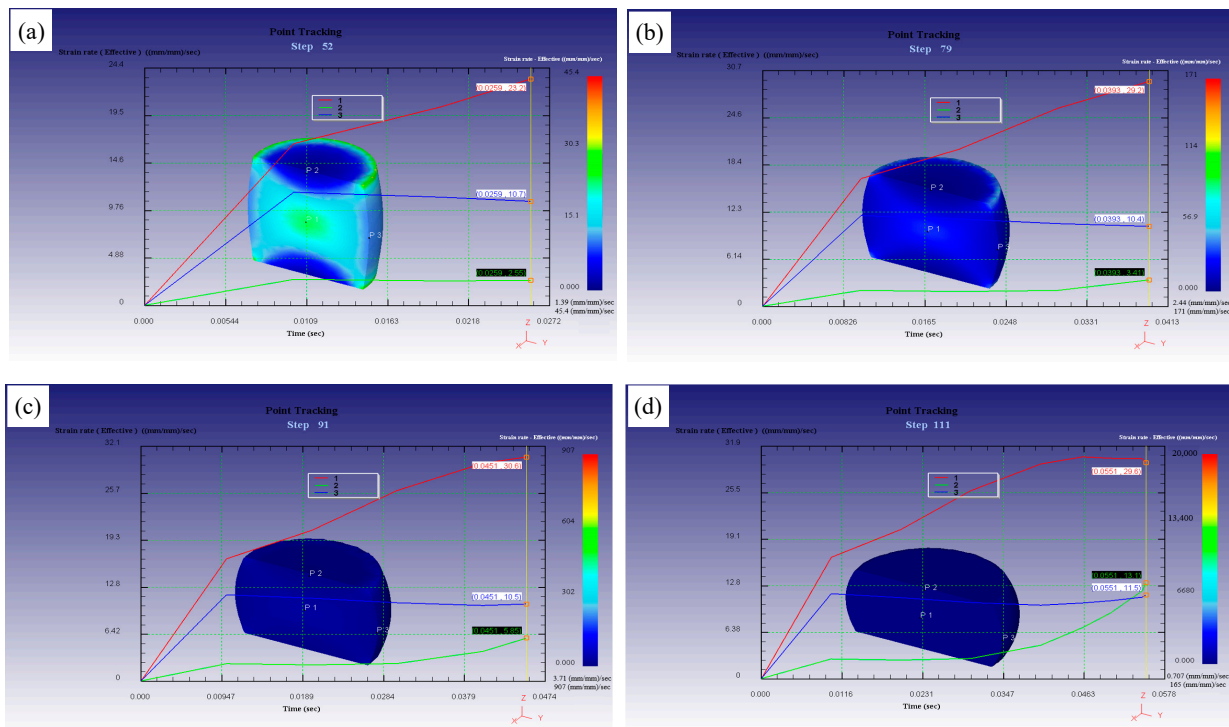
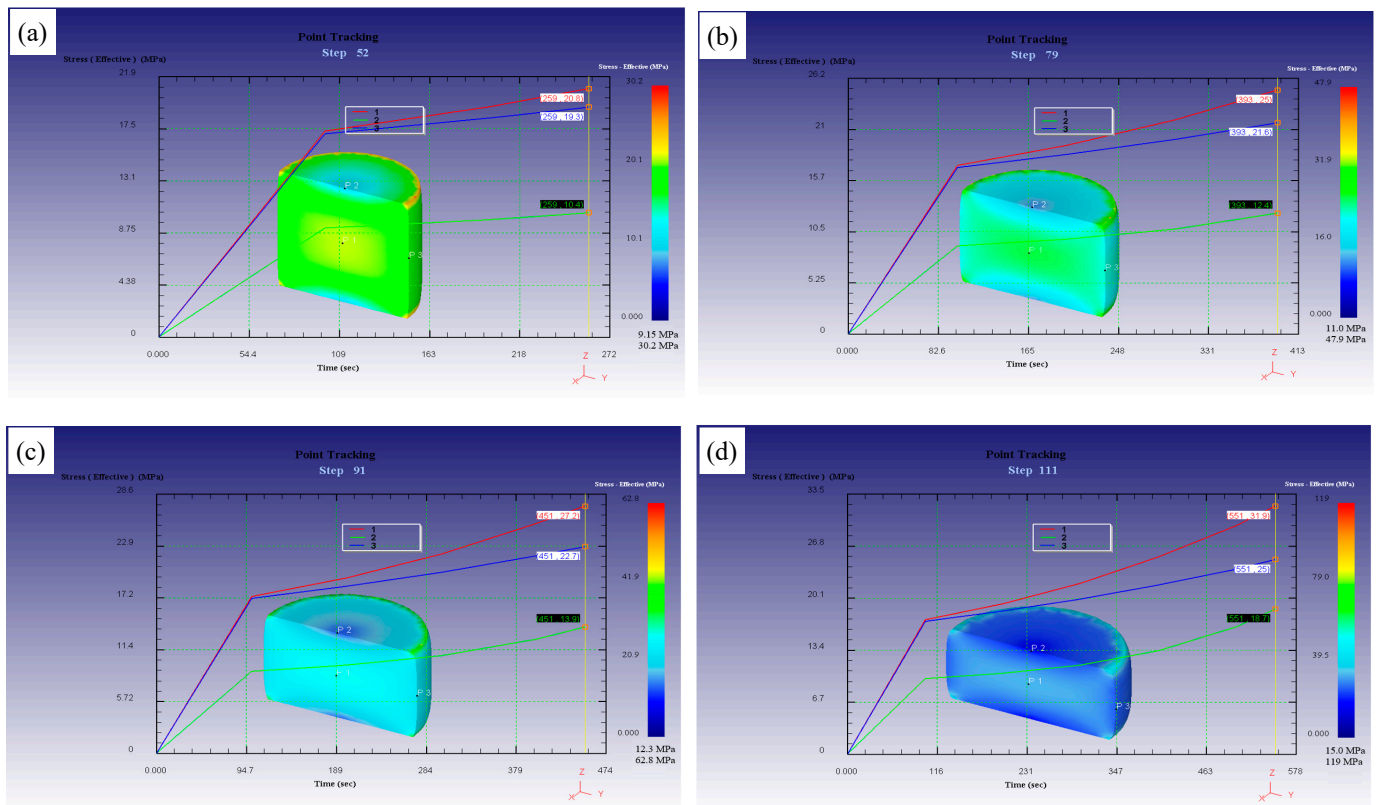


Figure 17. Effective strain rate field of the deformed samples at  $986\text{ }^{\circ}\text{C}/10\text{ s}^{-1}$ : (a) 0.3, (b) 0.5, (c) 0.6, and (d) 0.8.

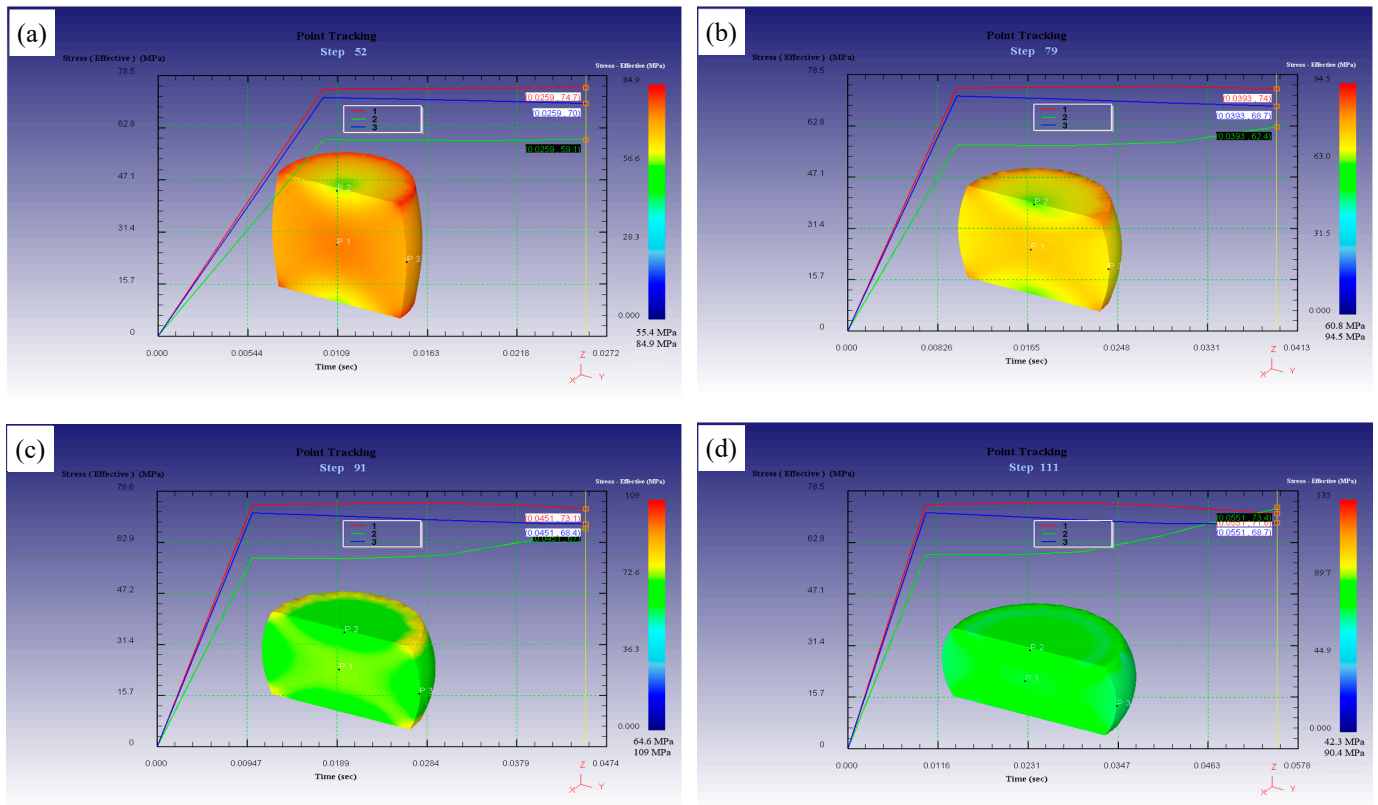
### 3.5.4. Effective Stress Field Simulation

Figure 18 depicts the simulation of the thermal compression effective stress field under the deformation condition of  $986\text{ }^{\circ}\text{C}/0.001\text{ s}^{-1}$ . It can be found that the evolution of the effective stress of the sample was similar to the evolution of the effective strain rate, which rose slowly after rising rapidly, and  $P1 > P3 > P2$  after compression. With the increase in strain, the effective stress increased slightly, and the difference in the effective stress between the easy deformation region and the hard deformation region is not large, indicating that the samples had good stability and uniform flow during compression under this deformation condition.



**Figure 18.** Effective stress field of the deformed samples at  $986\text{ }^{\circ}\text{C}/0.001\text{ s}^{-1}$ : (a) 0.3, (b) 0.5, (c) 0.6, and (d) 0.8.

For the effective stress field simulation with a deformation condition of  $986\text{ }^{\circ}\text{C}/10\text{ s}^{-1}$ , as shown in Figure 19, the effective stress in each region increased rapidly and then tended to be gentle or slightly decreased, which may be due to the fact that as the compression progressed to a certain degree, the softening behavior appeared in the sample, and the effective softening was equivalent to the effective hardening, reaching the dynamic equilibrium. When increasing the strain, the effective stress of the easy deformation region and intermediate deformation region decreased slightly, but the effective stress of the difficult deformation region increased. Moreover, the effective stress of P2 started to rise after it became flat. This may be because the strain rate was too large, resulting in a short deformation time, and the deformation of the difficult deformation region was not obvious, which resulted in a larger deformation resistance, so its effective stress increased.



**Figure 19.** Effective stress field of the deformed samples at  $986\text{ }^{\circ}\text{C}/10\text{ s}^{-1}$ : (a) 0.3, (b) 0.5, (c) 0.6, and (d) 0.8.

#### 4. Conclusions

By using the optical microscope and FE simulation method, the hot deformation behavior in the near  $\beta$  phase region of the forged TC21 alloy was studied in this work. The main conclusions are as follows:

(1) The flow behavior of the TC21 alloy is markedly affected by the hot processing parameters. The flow curves of the samples exhibited a flow-hardening behavior. With the increase in strain, the flow stress increased.

(2) Based on the flow curves and Arrhenius type equation, the constitutive equation at the peak stress of the TC21 alloy with a forged structure was constructed as follows:

$$\dot{\varepsilon} = 2.51 \times 10^{21} [\sinh(0.035\sigma_P)]^{3.09} \exp\left(-\frac{549121}{RT}\right)$$

(3) The processing maps at different strains were established on the basis of the dynamics materials model. A domain with peak efficiency of power dissipation was presented in the processing map, and the optimum hot working parameters were found to be  $986\text{ }^{\circ}\text{C}/10^{-3}\text{ s}^{-1}$ .

(4) In terms of the flow curves gained from hot compression tests and the hot processing maps of the TC21 alloy with a forged structure, the isothermal forging processing of the samples was simulated by the Deform-3D software. In the unstable region, the evolution of temperature field, strain field, and stress field in the deformed samples at different strains exhibited a similar trend: they were distributed symmetrically along the center line of the samples, and the center area of the samples was the highest, while the center area of the section was the lowest.

**Author Contributions:** Conceptualization, X.J. and Q.T.; methodology, X.J.; software, Y.T.; validation, C.H., M.W. and R.L.; formal analysis, Q.T.; investigation, X.J.; resources, X.J.; data curation, Q.T.; writing—original draft preparation, X.J.; writing—review and editing, Y.T.; visualization, Q.T.; supervision, Q.T.; project administration, C.H.; funding acquisition, C.H. All authors have read and agreed to the published version of the manuscript.

**Funding:** This research received no external funding.

**Data Availability Statement:** Not applicable.

**Acknowledgments:** This research was funded by The Science and Technology Projects of Guizhou Province (Grant Nos. [2021]310, YQK [2023]009, and [2022]050).

**Conflicts of Interest:** The authors declare no conflict of interest.

## References

1. Shao, H.; Shan, D.; Zhao, Y.Q.; Ge, P.; Zeng, W.D. Accordance between fracture toughness and strength difference in TC21 alloy with equiaxed microstructure. *Mater. Sci. Eng. A* **2016**, *664*, 10–16. [[CrossRef](#)]
2. Tan, C.S.; Sun, Q.Y.; Zhang, G.J.; Zhao, Y.Q. Remarkable increase in high-cycle fatigue resistance in a titanium alloy with a fully lamellar microstructure. *Int. J. Fatigue* **2020**, *138*, 105724. [[CrossRef](#)]
3. Elshaer, R.N.; Ibrahim, K.M. Effect of cold deformation and heat treatment on microstructure and mechanical properties of TC21 Ti alloy. *Trans. Nonferr. Metal. Soc. China* **2020**, *30*, 1290–1299. [[CrossRef](#)]
4. Wang, Y.S.; Yang, G.; Zhang, S.N.; Xiu, S.C. Effect of crystal orientation on micro-stress distribution in a damage-tolerant titanium alloy TC21. *J. Alloys Compd.* **2022**, *924*, 166637. [[CrossRef](#)]
5. Zhu, Y.C.; Zeng, W.D.; Feng, F.; Sun, Y.; Han, Y.F.; Zhou, Y.G. Characterization of hot deformation behavior of as-cast TC21 alloy using processing map. *Mater. Sci. Eng. A* **2011**, *528*, 1757–1763. [[CrossRef](#)]
6. Wang, K.; Wu, M.Y.; Yan, Z.B.; Li, D.R.; Xin, R.L.; Liu, Q. Dynamic restoration and deformation heterogeneity during hot deformation of a duplex-structure TC21 alloy. *Mater. Sci. Eng. A* **2018**, *712*, 440–452. [[CrossRef](#)]
7. Wang, K.; Wu, M.Y.; Ren, Z.; Zhang, Y.; Xin, R.L.; Liu, Q. Static globularization and grain morphology evolution of  $\alpha$  and  $\beta$  phases during annealing of hot-rolled TC21 alloy. *Trans. Nonferr. Met. Soc. China* **2021**, *31*, 2664–2676. [[CrossRef](#)]
8. Zhang, J.Q.; Xu, X.Y.; Xue, J.Y.; Liu, S.N.; Deng, Q.H.; Li, F.; Ding, J.; Wang, H.; Chang, H. Hot deformation characteristics and mechanism understanding of Ti-6Al-2Sn-4Zr-6Mo titanium alloy. *J. Mater. Res. Technol.* **2022**, *20*, 2591–2610. [[CrossRef](#)]
9. Qiu, Q.; Wang, K.L.; Li, X.; Wang, J.; Gao, X.; Zhang, K.M. Hot deformation behavior and processing parameters optimization of SP700 titanium alloy. *J. Mater. Res. Technol.* **2021**, *15*, 3078–3087. [[CrossRef](#)]
10. Gao, P.F.; Zhan, M.; Fan, X.G.; Lei, Z.N.; Cai, Y. Hot deformation behavior and microstructure evolution of TA15 titanium alloy with nonuniform microstructure. *Mater. Sci. Eng. A* **2017**, *689*, 243–251. [[CrossRef](#)]
11. Li, C.M.; Huang, L.; Li, C.L.; Hui, S.X.; Yu, Y.; Zhao, M.J.; Guo, S.Q.; Li, J.J. Research progress on hot deformation behavior of high-strength  $\beta$  titanium alloy: Flow behavior and constitutive model. *Rare Met.* **2022**, *41*, 1434–1455. [[CrossRef](#)]
12. Wang, J.; Wang, K.L.; Lu, S.Q.; Li, X.; OuYang, D.L.; Qiu, Q. Softening mechanism and process parameters optimization of Ti-4.2Al-0.005B titanium alloy during hot deformation. *J. Mater. Res. Technol.* **2022**, *17*, 1842–1851. [[CrossRef](#)]
13. Li, J.L.; Wang, B.Y.; Huang, H.; Fang, S.; Chen, P.; Shen, J.X. Unified modelling of the flow behavior and softening mechanism of a TC6 titanium alloy during hot deformation. *J. Alloys Compd.* **2018**, *748*, 1031–1043. [[CrossRef](#)]
14. Zhao, Y.L.; Li, B.L.; Zhu, Z.S.; Nie, Z.R. The high temperature deformation behavior and microstructure of TC21 alloy. *Mater. Sci. Eng. A* **2010**, *527*, 5360–5367. [[CrossRef](#)]
15. Zhu, Y.C.; Zeng, W.D.; Liu, J.L.; Zhao, Y.Q.; Zhou, Y.G.; Yu, H.Q. Effect of processing parameters on the hot deformation behavior of as-cast TC21 alloy. *Mater. Des.* **2012**, *33*, 264–272. [[CrossRef](#)]
16. Wang, Y.S.; Xiu, S.C.; Zhang, S.N.; Jiang, C.Y. Effect of grinding parameters on microstructure evolution of TC21 alloy with bimodal starting microstructure. *J. Alloys Compd.* **2020**, *831*, 154882. [[CrossRef](#)]
17. Zheng, X.Y.; Wang, K.; Zhang, C.; Xin, R.L.; Liu, Q. Evolution mechanism of lamellar  $\alpha$  and interlayered  $\beta$  during hot compression of TC21 alloy with a widmanstätten structure. *Chin. J. Aeronaut.* **2022**, *35*, 475–483. [[CrossRef](#)]
18. Shi, Z.F.; Guo, H.Z.; Liu, R.; Wang, X.C.; Yao, Z.K. Microstructure and mechanical properties of TC21 alloy by near-isothermal forging. *Trans. Nonferr. Met. Soc. China* **2015**, *25*, 72–79. [[CrossRef](#)]
19. Li, H.H.; Wang, K.; Xin, L.P.; Xin, R.L.; Liu, Q. Effect of hot rolling and annealing on phase component, recrystallization, and mechanical properties of TC21 alloy. *J. Mater. Eng. Perform.* **2022**, *31*, 2496–2508. [[CrossRef](#)]
20. Goetz, R.L.; Semiatin, S.L. The adiabatic correction factor for deformation heating during the uniaxial compression test. *J. Mater. Eng. Perform.* **2001**, *10*, 710–717. [[CrossRef](#)]
21. Mataya, M.C.; Sackschewsky, V.E. Effect of internal heating during hot compression on the stress-strain behavior of alloy 304L. *Metall. Mater. Trans. A* **1994**, *25*, 2737. [[CrossRef](#)]
22. Devadas, C.; Baragar, D.; Ruddle, G. The thermal and metallurgical state of steel strip during hot rolling: Part II. Factors influencing rolling loads. *Metall. Trans. A* **1991**, *22*, 321. [[CrossRef](#)]

23. Lu, H.T.; Li, D.Z.; Li, S.Y.; Chen, Y.A. Hot deformation behavior of Fe-27.34Mn-8.63Al-1.03C lightweight steel. *Int. J. Miner. Metall. Mater.* **2023**, *30*, 734–743. [[CrossRef](#)]
24. Mollaei, N.; Fatemi, S.M.; Aboutalebi, M.R.; Razavi, S.H.; Bednarczyk, W. Dynamic recrystallization and deformation behavior of an extruded Zn-0.2Mg biodegradable alloy. *J. Mater. Res. Technol.* **2022**, *19*, 4969–4985. [[CrossRef](#)]
25. Tan, Y.B.; Liu, W.C.; Yuan, H.; Liu, R.P.; Zhang, X.Y. On the phenomenon of stress drop during hot deformation of ZrTiAlV alloy. *Metall. Mater. Trans. A* **2013**, *44*, 5284–5288. [[CrossRef](#)]
26. Philippart, I.; Rack, H.J. High temperature dynamic yielding in metastable Ti-6.8Mo-4.5Fe-1.5Al alloy. *Mater. Sci. Eng. A* **1998**, *243*, 196–200. [[CrossRef](#)]
27. Wang, L.; Li, W.; Luan, S.Y.; Jin, P.P.; Wang, J.H.; Ren, Q.L.; Zhu, L. Study on hot deformation behavior of as-cast Ti-5Al-5Mo-5V-1Cr-1Fe titanium alloy in ( $\alpha+\beta$ ) phase region. *Mater. Today Commun.* **2023**, *35*, 105797. [[CrossRef](#)]
28. Tan, Y.B.; Ji, L.Y.; Duan, J.L.; Liu, W.C.; Zhang, J.W.; Liu, R.P. A Study on the Hot Deformation Behavior of 47Zr-45Ti-5Al-3V Alloy with Initial Lamellar  $\alpha$  Structure. *Metall. Mater. Trans. A* **2016**, *47*, 5974–5984. [[CrossRef](#)]
29. Niu, Y.X.; Hou, J.; Ning, F.K.; Chen, X.R.; Jia, Y.H.; Le, Q.C. Hot deformation behavior and processing map of Mg-2Zn-1Al-0.2RE alloy. *J. Rare Earth.* **2020**, *38*, 665–675. [[CrossRef](#)]
30. Liu, J.J.; Wang, K.L.; Lu, S.Q.; Gao, X.Y.; Li, X.; Zhou, F. Hot deformation behavior and processing map of Zr-4 alloy. *J. Nucl. Mater.* **2020**, *531*, 151993. [[CrossRef](#)]
31. Tan, Y.B.; Yang, L.H.; Duan, J.L.; Liu, W.C.; Zhang, J.W.; Liu, R.P. Effect of initial grain size on the hot deformation behavior of 47Zr-45Ti-5Al-3V alloy. *J. Nucl. Mater.* **2014**, *454*, 413–420. [[CrossRef](#)]
32. Tan, Y.B.; Ma, Y.H.; Zhao, F. Hot deformation behavior and constitutive modeling of fine grained Inconel 718 superalloy. *J. Alloys Compd.* **2018**, *741*, 85–96. [[CrossRef](#)]
33. Li, C.M.; Huang, L.; Zhao, M.J.; Guo, S.Q.; Li, J.J. Hot deformation behavior and mechanism of a new metastable  $\beta$  titanium alloy Ti-6Cr-5Mo-5V-4Al in single phase region. *Mater. Sci. Eng. A* **2021**, *814*, 141231. [[CrossRef](#)]
34. Luo, J.; Ye, P.; Li, M.Q.; Liu, L.Y. Effect of the alpha grain size on the deformation behavior during isothermal compression of Ti-6Al-4V alloy. *Mater. Des.* **2015**, *88*, 32–40. [[CrossRef](#)]
35. Ebrahimpourhandi, B.; Mahmudi, R. Hot deformation constitutive analysis and processing maps of the as-cast and wrought Mg-2.5Gd-0.5Zr alloy. *J. Alloys Compd.* **2023**, *942*, 169132. [[CrossRef](#)]
36. Liu, P.; Zhang, R.; Yuan, Y.; Cui, C.Y.; Zhou, Y.Z.; Sun, X.F. Hot deformation behavior and workability of a Ni-Co based superalloy. *J. Alloys Compd.* **2020**, *831*, 154618. [[CrossRef](#)]
37. Jiang, H.T.; Tian, S.W.; Guo, W.Q.; Zhang, G.H.; Zeng, S.W. Hot deformation behavior and deformation mechanism of two TiAl-Mo alloys during hot compression. *Mater. Sci. Eng. A* **2018**, *719*, 104–111. [[CrossRef](#)]
38. Liu, F.; Ma, J.M.; Peng, L.J.; Huang, G.J.; Zhang, W.J.; Xie, H.F.; Mi, X.J. Hot deformation behavior and microstructure evolution of Cu-Ni-Co-Si alloys. *Materials* **2020**, *13*, 2042. [[CrossRef](#)]
39. Tan, Y.B.; Duan, J.L.; Yang, L.H.; Liu, W.C.; Zhang, J.W.; Liu, R.P. Hot deformation behavior of Ti-20Zr-6.5Al-4V alloy in the  $\alpha+\beta$  and single  $\beta$  phase field. *Mater. Sci. Eng. A* **2014**, *609*, 226–234. [[CrossRef](#)]
40. Wu, H.; Liu, M.X.; Wang, Y.; Huang, Z.Q.; Tan, G.; Yang, L. Experimental study and numerical simulation of dynamic recrystallization for a FGH96 superalloy during isothermal compression. *J. Mater. Res. Technol.* **2020**, *9*, 5090–5104. [[CrossRef](#)]
41. Singh, G.; Souza, P.M. Hot deformation behavior of a novel alpha + beta titanium alloy TIMETAL<sup>®</sup>407. *J. Alloys Compd.* **2023**, *935*, 167970. [[CrossRef](#)]

**Disclaimer/Publisher’s Note:** The statements, opinions and data contained in all publications are solely those of the individual author(s) and contributor(s) and not of MDPI and/or the editor(s). MDPI and/or the editor(s) disclaim responsibility for any injury to people or property resulting from any ideas, methods, instructions or products referred to in the content.